Article:
Cheng, M., Zhao, X. and Li, G.-J. (2026) An image-to-image translation model for ultra-fast performance prediction of permanent magnet synchronous machines. IET Electric Power Applications, 20 (1). e70161. ISSN: 1751-8660

https://doi.org/10.1049/elp2.70161

IET Electric Power Applications

WILEY

The Institution of Engineering and Technology

ORIGINAL RESEARCH OPEN ACCESS

An Image-to-Image Translation Model for Ultra-Fast Performance Prediction of Permanent Magnet Synchronous Machines

Mengyu Cheng[1] | Xing Zhao[1] | Guangjin Li[2]

[1]School of Physics, Engineering and Technology, University of York, York, UK | [2]School of Electrical and Electronic Engineering, University of Sheffield, Sheffield, UK

Correspondence: Xing Zhao (xing.zhao@york.ac.uk)

Received: 12 January 2026 | **Revised:** 12 February 2026 | **Accepted:** 25 February 2026

Keywords: electric motors | electromagnetic fields | learning (artificial intelligence)

ABSTRACT

Recent advancements in artificial intelligence (AI) and deep learning (DL) have shown great potential in accelerating computational tasks. Notably, image-to-image translation (I2I) has gained significant attention due to its broad applications in computer vision and image processing problems. This paper presents a data-driven I2I model based on conditional generative adversarial networks (cGAN) to predict the performance of an interior permanent magnet synchronous machine (IPMSM). The generator of the cGAN can plot tangential and radial magnetic flux density maps from the input cross-sectional images of an IPMSM with varying geometric features, dimensions, pole-slot configurations and excitations. Additionally, a comparison is made between traditional cGAN networks and a modified multidomain version that incorporates a physics-informed loss function. Model test shows that the proposed method significantly reduces computation time. For a single design, the improvement of evaluation speed is approximately 90.23% compared to the FEA simulation. Besides, the multidomain evaluative model can reduce training time consumption whilst improving the prediction accuracy. Experimental validation indicates that the predicted magnetic flux density maps have an average error of less than 0.13% compared to FEA results. Furthermore, post-processing the generated images enables the calculation of the torque, flux linkage and induced voltage of the IPMSM. The accuracy of performance calculation using the I2I model is also verified against data obtained from FEA software.

1 | Introduction

In modern society, electric machines are the core of driving industrial automation, transportation and household appliances, and they are one of the largest electricity consumers in the world [1]. The design and optimisation of electric machines aim to develop practical designs that meet specific performance requirements whilst minimising cost and environmental impacts [2]. This work often involves multidisciplinary analysis considering dimensions, topologies, excitation methods, materials and operating conditions. Finite element analysis (FEA) is widely used in this work due to its exceptional accuracy and flexibility in handling complex geometries. FEA provides detailed insight into the electromagnetic and mechanical behaviours of electric machines and is essential for computing multiphysics field solutions [3]. However, the high computational cost associated with FEA presents a considerable challenge, particularly when simulating large numbers of individuals [4]. Therefore, researchers are exploring suitable data-driven methods that have the potential to replace FEA in the machine design optimisation process [5].

Over recent years, deep learning (DL) models, a subset of machine learning (ML) that utilises multilayered neural networks, have shown considerable promise in this area due to their ability to extract local features from high-dimensional data and cover a broader range of design variables [6]. Notably, some studies employing convolutional neural networks (CNNs) [7–11] and generative adversarial networks (GANs) [12–14] have developed robust analytical models by extracting geometric features from machine images, enabling them to circumvent the limitations on the number of degrees of freedom (DoFs). Specifically, GAN-based image-to-image translation (I2I) models for predicting magnetic field distributions have proven effective in accurately reflecting machine performance with a relatively small number of training samples.

This paper develops a novel data-driven I2I model based on a conditional generative adversarial network (cGAN) with a modified physics-informed loss function for predicting the performance of an interior permanent magnet synchronous machine (IPMSM). This approach significantly reduces computation time compared to FEA simulation. Through I2I [15], the generator of the cGAN predicts the tangential and radial magnetic flux density from the input cross-sectional image of IPMSMs, considering various geometric dimensions, pole-slot configurations, and current densities. The predictions can be used to calculate the machine's torque, flux linkage and induced voltage.

2 | Methodology

The overall procedure of the study is depicted in Figure 1. The workflow involved obtaining cross-sectional images of an IPMSM under various conditions, data preprocessing, training a cGAN with images that contain the information of a series of variables and the corresponding magnetic flux density distribution maps obtained through FEA simulation, saving the generator of the network to predict magnetic flux density distributions of new input design, and postprocessing to evaluate machines' performance.

2.1 | Data Design

Given that the study aims to build a surrogate model that matches the accuracy and flexibility of FEA, the information constraints that the input data contain should be as adequate as possible. Existing studies applying DL models that use images as input data allow models to bypass the limitations on the degrees of freedom (DoFs) encountered in other ML models [16–22] that use variable vectors. However, most studies only use images to express machines' geometric features, which is insufficient for a competent model. Therefore, the input data in this work is manually designed cross-sectional images of IPMSMs that encapsulate information on topologies, geometric parameters, material distribution and excitation.

In ref. [14], the authors divided the input into multiple RGB plots, using normalised definitions of colour warmth and coldness to encode current densities and relative permeabilities of materials within the input images. However, using a nonlinear definition of colour warmth and coldness complicates image processing and network learning. In this study, given that input images are read in RGB format, specific colours are directly used to represent different materials as shown in Figure 2a and Table 1. The linear RGB encoding is adopted to ensure a clear and numerically interpretable representation of material distributions and excitation, whilst more complex encoding schemes can be incorporated in future work if required. Specifically, the coil parts are represented by solid colours: red, green and blue for the three phases, respectively. The colour values and RMS current density are related as described in Equation (1).

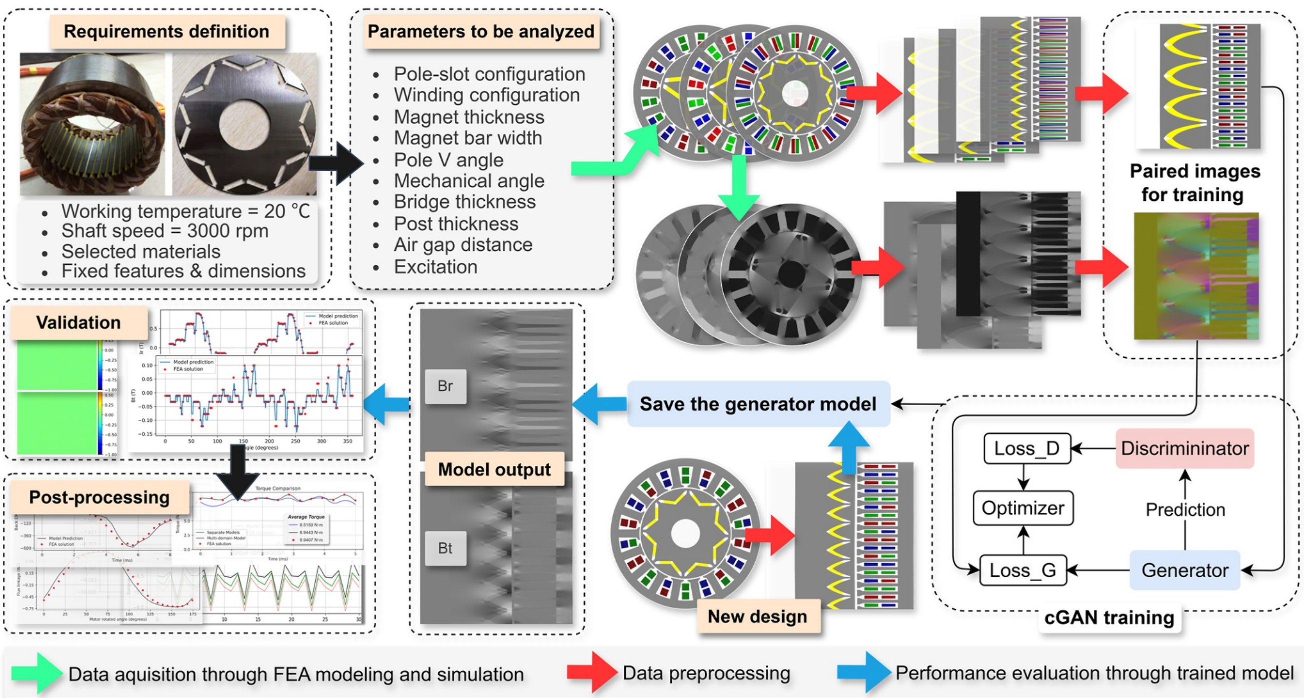

FIGURE 1 | The workflow of performance prediction of an IPMSM using I2I.

$$J = (\text{color}_I - \text{color}_{\text{zero}}) \times K, \tag{1}$$

where J $\left(\text{A}/\text{mm}^2\right)$ represents the RMS current density, color_I ranging from [0, 255] is the pixel colour value of the corresponding phase, $\text{color}_{\text{zero}} = 108$ is the baseline colour value, corresponding to $J = 0$, and K is a scaling constant.

2.2 | Training Sample Acquisition

The present study is based on a two-dimensional modelling framework, in which the influence of end windings is not explicitly considered. Although the cross-sectional images are manually designed in this study, the image generation process follows deterministic encoding rules and can be readily automated using parametric modelling tools. The training samples were acquired from Ansys Maxwell 2D by simulating an IPMSM with various geometric dimensions, pole-slot configurations and excitations. Each data set consists of four images: a cross-sectional image of the machine, an overall map of magnetic flux density distribution, a radial flux density map and a tangential flux density map.

The fixed geometrical parameters of the IPMSM are detailed in Table 2. The IPMSM features a fixed number of 18 slots, with the coil span designed according to the short-pitch winding principle, which helps to reduce harmonics in the IPMSMs [23] as described in Equation (2).

$$y = \left\lfloor \frac{N_s}{2p} \right\rfloor, \tag{2}$$

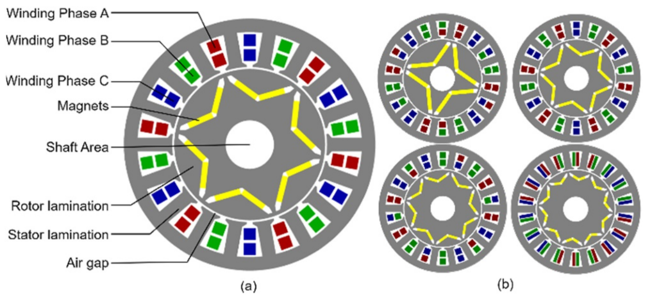

FIGURE 2 | Input data format. (a) The cross-sectional image design. (b) IPMSMs with different numbers of pole pairs.

where y is the number of slots the coil spans, N_s is the total number of slots and p is the number of pole pairs.

Four coil distributions were considered as depicted in Figure 2b. The training sample variables are outlined in Table 3. Each motor configuration was sampled at 15 different mechanical angles, representing a half cycle of magnetic field rotation. This sampling method prevents the same geometric configuration from corresponding to different magnetic flux density maps. Consequently, a total of 14,400 sample sets were obtained. The sampled current density range is intentionally selected to include high-excitation conditions, under which magnetic saturation may occur, ensuring that the generated flux density distributions inherently reflect saturation effects.

For acquiring magnetic flux density maps, some studies [13, 24, 25] have attempted to generate these maps using colour maps, such as the jet colour map, which is commonly used for visualising density. Similar to the expression of input excitation, this visualisation method requires three matrices (channels) to represent each magnetic flux density map. The nonlinear relationship between each pixel's red, green and blue values and the actual magnetic flux density values complicates postprocessing. Therefore, this study acquired magnetic flux density images in grayscale, establishing a linear relationship between the grayscale values and the corresponding magnetic flux density values.

2.3 | Data Pre-Processing

Before the model training, all images were converted from Cartesian coordinates to polar coordinates to facilitate the training process by eliminating blank spaces and reducing the complexity of arcuate features. The geometric images were read as three-channel RGB images, whereas the three magnetic flux density maps were read as single-channel grayscale images. As shown in Figure 1, these grayscale images were then concatenated into a three-channel image that can be read in RGB format. This pairing of a three-channel geometric image and a three-channel magnetic flux density image was used as input–output pairs for training. The relationship between the resultant magnetic flux density ($B_{\text{resultant}}$), the radial magnetic flux density (B_r) and the tangential magnetic flux density (B_t) is given by:

TABLE 1 | Design of IPMSMs' cross-sectional images.

Material	Part name	Colour display	RGB values
Vacuum	• Rotating band	White	(255, 255, 255)
	• Shaft		
	• Whole region		
Pure copper coil	• Winding phase A	Red	(color_I, 0, 0)
	• Winding phase B	Green	(0, color_I, 0)
	• Winding phase C	Blue	(0, 0, color_I)
Silicon steel 350-50A	• Rotor lamination	Grey	(128, 128, 128)
	• Stator lamination		
Neodymium magnets 30UH	• Magnets	Yellow	(255, 255, 0)

$$B_{\text{resultant}}{}^2 = B_r{}^2 + B_t{}^2. \quad (3)$$

This way, an encoder–decoder model can be sufficiently utilised for I2I, functioning with a single input and producing outputs in three domains. Given the clear numerical relationship between the three magnetic flux density maps, a corresponding loss function can be incorporated during training to enhance the model's performance. This approach leverages the structure of the GAN's generator to handle the complexity of multiple outputs whilst ensuring that the interrelated nature of the magnetic flux density maps is effectively captured and utilised in the training process.

2.4 | Training and Performance Evaluation

During the training, the generator of the proposed cGAN learns to predict the magnetic flux density distribution from the cross-sectional images of the IPMSM. The training is evaluated and monitored by comparing the generated magnetic flux density images with authentic images obtained from FEA simulations using a modified physics-informed loss function.

Once the loss function and real-time average error converge, the generator is saved as the predictive model. The generator predicts the corresponding magnetic flux density distributions by inputting cross-sectional images of IPMSMs with new design parameters. Since predicted magnetic flux density maps are initially grayscale images, they are converted to magnetic flux density values using a specific relationship between the pixel grayscale values and the corresponding magnetic flux density values. The conversion process is explained as follows:

$$B = B_{\min} + \left(\frac{B_{\max} - B_{\min}}{\text{color}_{\text{top}} - \text{color}_{\text{bot}}}\right) \times \left(\text{color}_{\text{pixel}} - \text{color}_{\text{bot}}\right), \quad (4)$$

where B is the magnetic flux density value, $B_{\min}$ is the minimum magnetic flux density, which is set to 0 T for overall flux density and set to −2.75 T for radial and tangential flux density, $B_{\max}$ is the maximum magnetic flux density, set to 2.75 T for all maps, $\text{color}_{\text{pixel}}$ is the pixel's grayscale value, ranging from 3 to 252 and $\text{color}_{\text{top}}$ and $\text{color}_{\text{bot}}$ are the upper and lower bounds of the grayscale values used for scaling.

After converting the grayscale images to magnetic flux density maps, the IPMSMs' performance is evaluated through some key metrics, including torque, magnetic flux linkage and induced voltage.

The torque of the IPMSM is calculated using the radial and tangential components of the magnetic flux density in the air gap. As mentioned previously, all images are first transformed from Cartesian to polar coordinates to facilitate this calculation. This conversion simplifies the extraction of magnetic flux density values in the air gap as the square images allow for easy retrieval of a circular line of magnetic flux densities corresponding to the air gap radius. The steps to calculate the torque using the Maxwell stress tensor (MST) are as follows: (1) Extract the magnetic flux density values from the air gap by retrieving the grayscale values from the column corresponding to the radius r in the polar coordinate image; (2) convert these grayscale values to magnetic flux density values using the Equation (4); (3) apply filters to smooth the magnetic flux density curves to ensure better continuity; (4) multiply the filtered radial and tangential magnetic flux density components and (5) integrate the product over the range of 0 to 2π to calculate the torque using MST. The torque T is given by:

$$T = \frac{Lr^2}{\mu_0} \int_0^{2\pi} B_r(\theta, r) B_t(\theta, r) d\theta, \quad (5)$$

where L is the stack length of the IPMSM, r is the radius of the air gap and μ_0 is the vacuum permeability.

It should be noted that the influence of magnetic saturation is implicitly considered in the proposed torque calculation. All training and validation data are generated using FEA with nonlinear magnetic material properties, which inherently captures magnetic saturation under different operating conditions. Consequently, the predicted radial and tangential magnetic flux density components already embed saturation effects.

The magnetic flux linkage through each phase is determined by integrating the flux densities in coil regions. The calculation of flux linkage involves summing the magnetic flux passing through each coil turn to obtain the total flux linkage. The flux linkage λ is given by:

$$\lambda = \sum_{i=1}^{N} \iint_A B_r \cdot dS, \quad (6)$$

TABLE 2 | Fixed geometrical parameters of the IPMSM.

Stator parameter	Value	Rotor parameter	Value
Stator length	90 mm	Stack length	90 mm
Slot number	18	Pole notch depth	0 mm
Outer diameter	130 mm	Magnet bridge	2 mm
Bore diameter	80 mm	Magnet layers	1
Tooth width	7 mm	Magnet segments	1
Slot depth	18 mm	Magnet gaps	0 mm
Tooth tip depth	1 mm	Airgap length	1 mm
Tooth tip angle	30°	Banding thickness	0 mm
Slot opening	3 mm	Shaft diameter	25 mm

TABLE 3 | Variables of training samples.

Variable	Min.	Max.
Number of pole pairs	4	10
Magnet thickness	2.5 mm	4.5 mm
V-angle between poles	125°	145°
Magnet bridge thickness	1.5 mm	4 mm
Magnet post thickness	0 mm	2 mm
Magnet separation	0 mm	1.5 mm
Magnet width	6 mm	24 mm
RMS current density	0 A/mm^2	25.8 A/mm^2

where N is the number of turns per coil and A is the coil plane through which the magnetic flux passes.

The induced voltage in the coil phases can be calculated using the variation of the phase flux linkage over time according to Faraday's Law of Induction.

3 | Network Architecture

To accurately predict magnetic flux density distributions from machine structural data, a tailored neural network architecture is essential. In this study, a conditional generative adversarial network is adopted. The cGAN framework is particularly well-suited for problems requiring precise spatial mappings between inputs and outputs, making it ideal for converting machine cross-sectional representations into detailed flux density maps.

GANs operate on the principle of adversarial training between two neural networks: the generator and the discriminator. The generator aims to produce synthetic data samples that are indistinguishable from real data, whereas the discriminator's role is to differentiate between real and generated data [26]. Based on this, cGANs extend the framework by conditioning the generator on additional input information, such as images, allowing cGANs to generate outputs that are more semantically meaningful and contextually accurate [27]. In this study, the network is trained with the generator aiming to create realistic magnetic flux density maps based on the input conditions of machine features, and the discriminator strives to evaluate the authenticity of the generated images.

3.1 | Generator

The generator employs a ResUnet architecture [28], as depicted in Figure 3, an encoder–decoder structure specifically designed to transform input cross-sectional images into accurate magnetic flux density maps. To ensure consistency and improve training stability, all images are resized to a fixed size of 512×512 pixels using antialiasing to maintain image quality. The pixel values are normalised to the range of $[-1, 1]$, with a mean and standard deviation of 0.5. The encoder begins with an initial residual convolution module (stride = 1), which prepares the data by extracting features relevant to the subsequent processing stages. Following the initial block, the architecture employs several layers of residual convolution.

As shown in Figure 4, each residual convolutional module consists of two consecutive convolutional layers with batch normalisation and Leaky ReLU activation, promoting feature extraction and learning hierarchical representations at progressively lower spatial resolutions. This modular architecture allows for flexibility in adjusting network depth and complexity according to the specific requirements of the image translation task [28].

In the decoder path, the architecture reverses the process using transposed convolutional layers combined with residual convolution modules. These decoding layers increase the spatial resolution of the feature maps whilst integrating information from the skip connections established during the encoding phase [29]. This process aims to recover spatial details lost during encoding and refine the generated output. Finally, the output layer produces the desired output image, where a hyperbolic tangent activation function ensures that the pixel values are scaled to the range $[-1, 1]$.

3.2 | Discriminator

The discriminator is designed to evaluate the authenticity of the magnetic flux density maps generated by the generator, determining whether they are realistic or not. It utilises a convolutional neural network for binary classification. Specifically, the input to the discriminator is a six-channel image formed by concatenating the input cross-sectional machine images with either the real or generated magnetic flux density map along the channel dimension.

As illustrated in Figure 5, this concatenated image is passed through a series of convolutional layers, enabling the network to learn correlations between the geometry and the corresponding

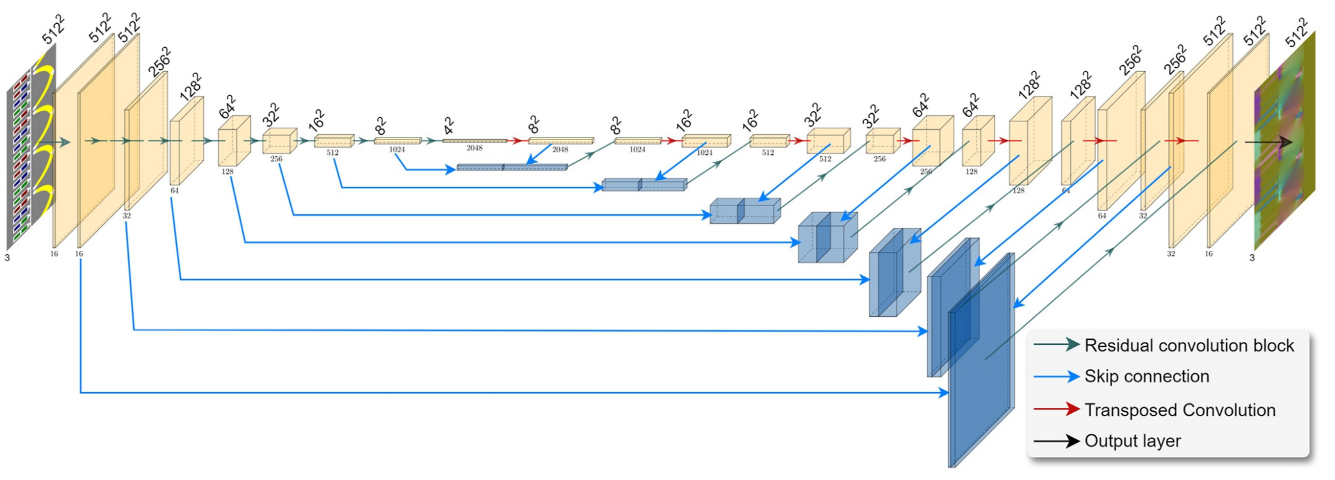

FIGURE 3 | The ResUnet architecture applied for the generator.

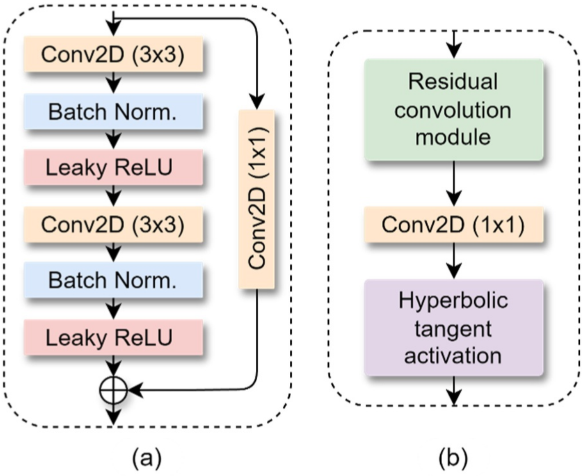

FIGURE 4 | Operation details of the generator. (a) Residual convolution module. (b) Output layer.

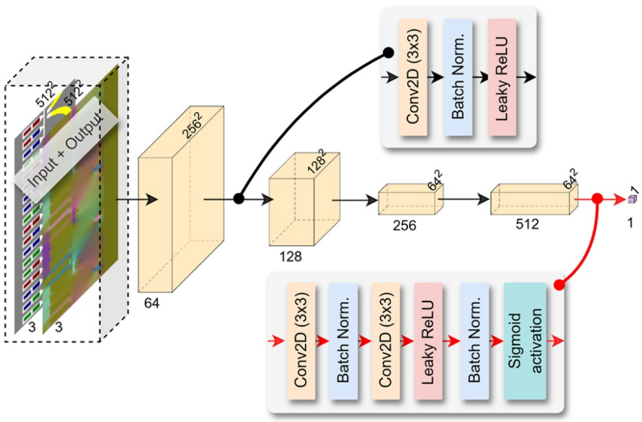

FIGURE 5 | Discriminator.

flux distribution. The output is a single scalar value representing the discriminator's confidence in the authenticity of the input flux map. By learning to distinguish between real and synthetic flux maps, the discriminator forces the generator to improve its predictions to deceive the discriminator, ultimately enhancing the realism and physical accuracy of the generated outputs.

3.3 | Loss Function

The loss function in the model combines traditional adversarial loss with physics-informed components to guide the generator's predictions more effectively. The adversarial loss encourages the generator to produce images indistinguishable from the real ones, whereas the physics-informed loss penalises deviations from known physical consistency and FEA results. This hybrid loss function ensures that the generated magnetic flux density maps are not only visually realistic but also physically accurate.

The adversarial loss ensures that the generator G produces images that the discriminator D cannot distinguish from real images. The loss can be written as Equations (7) and (8) for the discriminator, respectively.

$$\mathcal{L}_D = -\mathbb{E}_{x,y}[\log D(x,y)] - \mathbb{E}_{x,z}[\log(1 - D(x, G(x)))], \tag{7}$$

$$\mathcal{L}_{\text{adv}} = -\mathbb{E}_{x,z}[\log D(x, G(x))], \tag{8}$$

where x represents the input annotations, y represents the real images and z represents the generated images $G(x)$.

Additionally, the generator incorporates an L1 loss to ensure the generated images are close to the real pixel values. It is defined as follows:

$$\mathcal{L}_{\text{L1}} = \mathbb{E}_{x,y,z}[\ \| G(x) - y \|_1]. \tag{9}$$

In addition to the fundamental loss, the physics-informed components are gradient loss, channel relation loss and torque loss. These components are crucial in this application as they embed domain-specific knowledge into the training process, improving the model's effectiveness in predicting machines' performance characteristics. Gradient loss enhances the similarity of gradients between the generated image and the real image. This is achieved by calculating the gradient along the x- and y-axes using the Sobel operator. The average absolute error between the predicted and actual solutions then defines the function:

$$\mathcal{L}_{\text{grad}} = \mathbb{E}_{x,y,z}[\ \| \nabla G(x) - \nabla y \|_1]. \tag{10}$$

The channel relation loss ensures that the generated magnetic flux densities adhere to the physical relationships between the channels as expressed in Equation (3). For the generated image's red, green and blue channels, this loss is defined as follows:

$$\mathcal{L}_{\text{relation}} = \mathbb{E}_{x,y,z}\left[\|G_r(x)^2 + G_g(x)^2 - G_b(x)^2\|_1\right]. \tag{11}$$

The torque loss ensures that the torque computed from the generated images is close to the torque calculated from the real images. This is achieved by obtaining the flux density values from the images during the training process and then comparing the resulting torque values calculated through MST:

$$\mathcal{L}_{\text{torque}} = \mathbb{E}_{x,y,z}\left[\|T_{\text{gen}} - T_{\text{real}}\|_1\right]. \tag{12}$$

The final generator loss function combines these components with appropriate weighting factors:

$$\mathcal{L}_G = \mathcal{L}_{\text{adv}} + \lambda_1 \mathcal{L}_{\text{L1}} + \lambda_2 \mathcal{L}_{\text{grad}} + \lambda_3 \mathcal{L}_{\text{relation}} + \lambda_4 \mathcal{L}_{\text{torque}}, \tag{13}$$

where λ_1, λ_2, λ_3, and λ_4 are hyperparameters that balance the contributions of each loss component. The implementation details used in this study are summarised in Table 4.

The weighting coefficients of the loss terms were selected based on preliminary experiments. Their values were chosen to balance the relative contributions of the adversarial, pixel-wise and physics-informed loss components, ensuring stable training convergence and accurate prediction of both magnetic field distributions and derived performance quantities.

TABLE 4 | Key training hyperparameters of the model.

Hyperparameter	Value
Optimiser	Adam
Generator learning rate	0.0003
Discriminator learning rate	0.000001
Batch size	10
Weight of L1 loss (λ_1)	1
Weight of gradient loss (λ_2)	0.3
Weight of relation loss (λ_3)	0.3
Weight of torque loss (λ_4)	0.3

4 | Results

4.1 | I2I Model Training and Testing

As shown in Figure 6, the training is monitored for loss convergence, indicating robust competition between the generator and the discriminator during the training process, which ensures the model is well-tuned to the data. At the same time, the model's effectiveness for each epoch was roughly estimated and monitored by calculating the average prediction error for a randomly selected batch of test data. The generated images are evaluated using the mean absolute error (MAE) and root mean squared error (RMSE) metrics in comparison to FEA-generated magnetic flux density maps. These metrics were measured with all images normalised to values in the range [−1, 1] for each pixel. The network is trained on a dataset of 14,400 image groups, each consisting of a machine cross-sectional image and its corresponding magnetic density maps under different geometrical parameters, pole-slot configurations and current densities. The network converges after about 260 epochs. The training duration is approximately 282 h (63.3 min per epoch) on an NVIDIA RTX 4070 Ti GPU.

The trained model took around 2.71 s to produce 15 prediction images for one new machine design, whereas Ansys Maxwell took 27.73 s (including 5.72 s for configuration initialisation), indicating a speed improvement of 90.23%. Following this, 95 new randomly selected machine designs were used for further validation. With the same rules for acquiring training data, each design has 15 images with different mechanical angles, resulting in 1425 sets of images used for testing. Prediction results of an example test input are shown in Figure 7. Although the training phase is computationally demanding, it is performed offline and enables ultrafast inference, making the proposed approach particularly suitable for applications involving repeated performance evaluations.

4.2 | Comparative Study of Models

To validate the necessity of the proposed multidomain model, the accuracy of using two separate networks to predict the radial magnetic flux density (B_r) maps and the tangential magnetic flux density (B_t) maps independently is also evaluated. In this alternative approach, the network structure remains unchanged. Still, each grayscale magnetic flux density map is

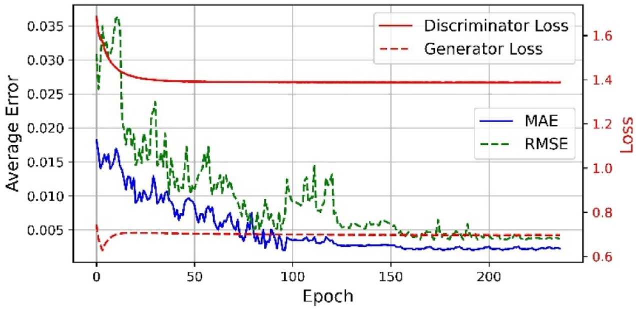

FIGURE 6 | Loss and error record during model training.

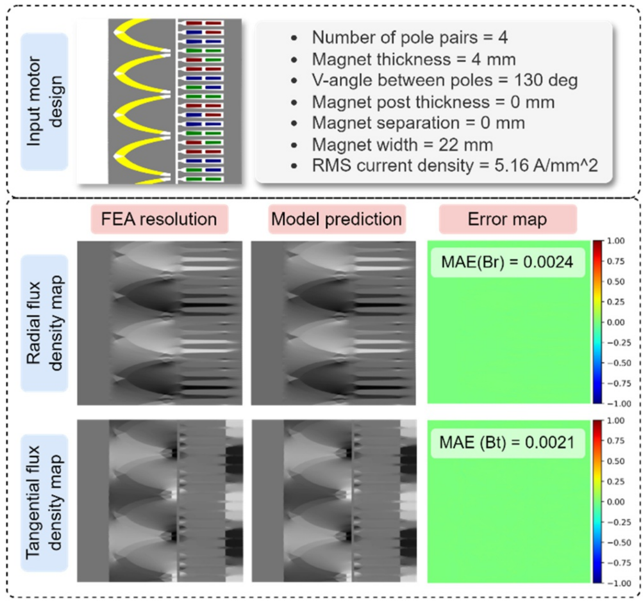

FIGURE 7 | Predicted flux densities of a tested IPMSM compared to FEA resolutions.

replicated three times and then combined into a single three-channel image for training. The loss function associated with torque calculation and numerical relationships between the magnetic flux density maps is removed.

The kernel density estimation plots of MAE and RMSE results for all 1425 test image sets are shown in Figure 8. The average and maximum values of the networks' prediction errors are summarised in Table 5. It can be observed that the proposed physics-informed multidomain model has better accuracy compared to separate networks.

Figure 9 illustrates the distribution of test sample features and the prediction's MAE for each test sample. Statistically, 99.7% of all test results have an MAE of less than 2.60 e^{-3} (0.13%) for the proposed multidomain model.

4.3 | Flux Density Validation

To further assess the model's accuracy in predicting magnetic flux density, attention is paid to values from the centre of the air gap. The proposed model particularly emphasises the flux density in the centre of the air gap in the loss function, which is designed to track torque calculation accuracy. The generated magnetic flux density maps are validated by selecting specific columns corresponding to the air gap and comparing the grayscale values converted to flux density values using Equation (3). The magnetic flux density values at the centre of the air gap are extracted and compared with those obtained from the FEA counterparts. This comparison ensures the model's accuracy in replicating the physical characteristics of the IPMSM's magnetic field distribution. For instance, the predicted flux densities for the new machine design, as shown in Figure 7, match the FEA results as depicted in Figure 10.

4.4 | Electromagnetic Torque Validation

The torque is calculated using the radial and tangential components of the magnetic flux density in the air gap. The previously converted magnetic density maps facilitate this calculation. By integrating the product of Br and Bt over the circumference of the air gap, the torque is obtained using Equation (5).

For the design in Figure 7, the proposed multidomain network and separate networks for Br and Bt are tested. Figure 11 compares the predicted torque values and the FEA results for the new motor design. It can be observed that the proposed method has better accuracy on torque prediction compared to separate models, and the predicted values of the proposed model closely match those obtained from FEA simulations.

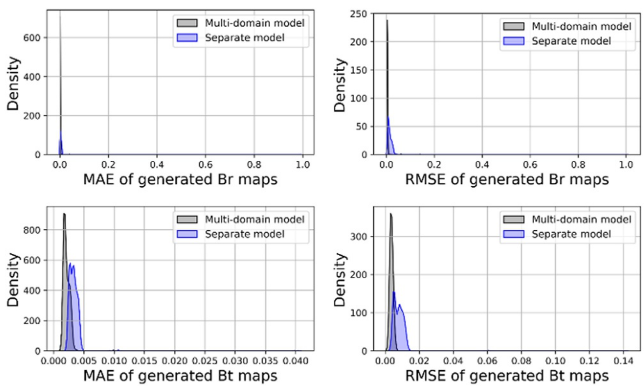

FIGURE 8 | Prediction errors' probability density distribution.

4.5 | Flux Linkage Validation

The flux linkage (λ) is obtained by sampling the radial flux density at multiple points in the coil regions in the image and then calculating it using Equation (6). The predicted results from the generated magnetic flux density maps are compared with values exported from FEA, showing a high degree of agreement. This demonstrates the model's effectiveness in predicting the flux linkage. Figure 12a shows the flux linkage comparison for the example design in Figure 7.

4.6 | Induced Voltage Validation

The induced voltage (V) in the coils is calculated using the variation of the flux linkage over time as the number of turns per coil is a predesigned constant. To validate the results throughout the periodicity, the predictions for each machine design can be expanded to 30 time points (mechanical angles), utilising the periodic symmetry of the predicted images. Figure 12b illustrates the comparison of the induced voltage between the model predictions and the FEA results for the example design in Figure 7.

4.7 | Generalisation to Unseen Topologies

To further evaluate the generalisation capability of the proposed model, prediction results for motor topologies not included in the training dataset are presented. As shown in Figure 13, the model is able to reproduce the main magnetic field distribution features of unseen topologies. However, when the structural difference from the training set increases, a degradation in prediction accuracy can be observed. This is mainly attributed to the domain shift between the training and testing samples, which is a common limitation of data-driven approaches. This limitation highlights the need for future research on training strategies that incorporate more diverse motor topologies to enhance the generalisation performance.

5 | Conclusion

This study presents a cGAN-based I2I model for predicting the magnetic performance of an IPMSM. The model predicts the magnetic flux density distributions from cross-sectional images of IPMSMs, incorporating varying geometric parameters, pole-slot number combinations and current densities, offering a

TABLE 5 | Prediction errors of different models (tesla).

Prediction		MAEavg	RMSEavg	MAEmax	RMSEmax
Multidomain model	B	2.53 e-3	4.94 e-3	3.36 e-3	1.89 e-2
	Br	2.31 e-3	4.55 e-3	2.78 e-3	2.02 e-2
	Bt	2.19 e-3	4.10 e-3	9.92 e-3	1.39 e-2
Separate Br model	Br	4.54 e-3	1.45 e-2	9.8 e-2	9.9 e-2
Separate Bt model	Bt	3.32 e-3	8.15 e-3	4.04 e-2	1.41 e-2

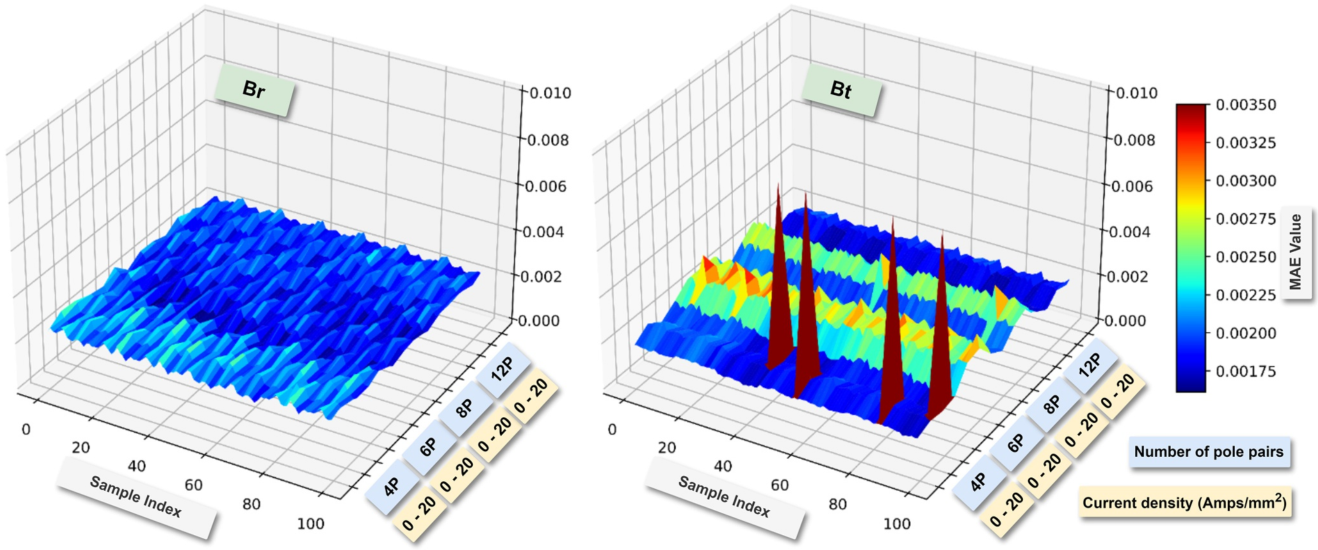

FIGURE 9 | The distribution of test sample features and MAE values.

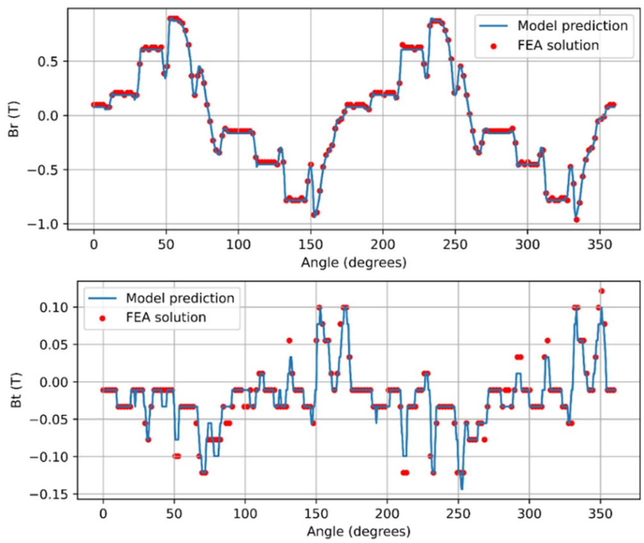

FIGURE 10 | Predicted flux densities at the centre of the air gap of the tested IPMSM compared to FEA results.

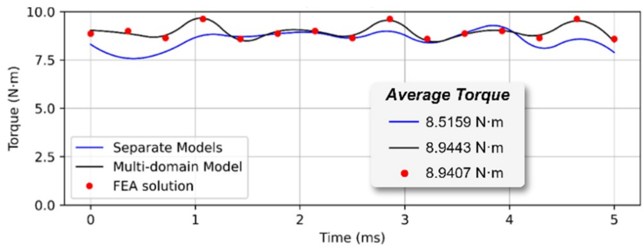

FIGURE 11 | Torque calculated through predicted flux densities compared to FEA results.

viable alternative to FEA methods. The key conclusions from this work are summarised as follows: (i) Effective prediction model: The proposed model effectively predicts magnetic flux density distributions with high accuracy. The error metrics indicate that the model's predictions are closely aligned with FEA results, demonstrating its reliability in replicating the physical characteristics of the IPMSM's magnetic field distribution. (ii) Reduced computation time: The computational

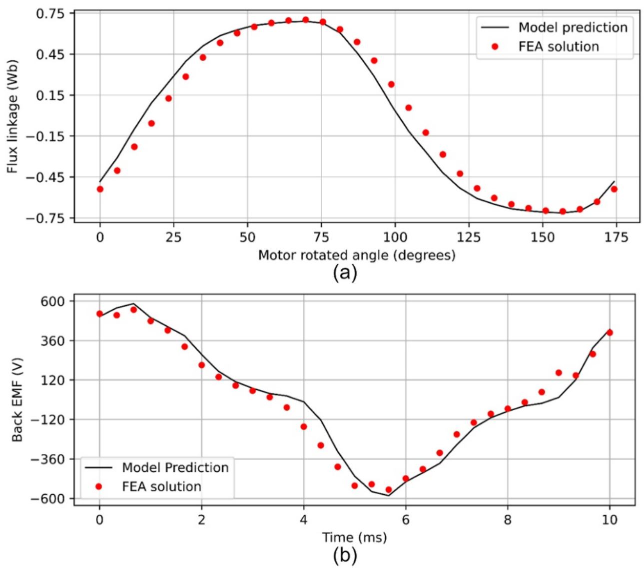

FIGURE 12 | Performance calculation of the tested design using model prediction compared to FEA results. (a) Flux linkage. (b) Induced voltage.

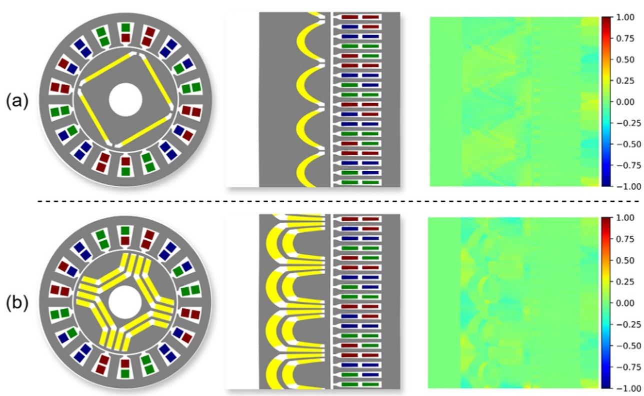

FIGURE 13 | Br prediction results for motors with different rotor topologies outside the training set. (a) Flat shaped IPMSM. (b) 2 layered U-shaped IPMSM.

speed of the proposed model is increased by approximately 90.23% compared to FEA simulations, making it particularly beneficial in situations involving multiple individuals or real-time performance evaluations. (iii) Accurate performance evaluation: Postprocessing the predicted generated images allows for accurate calculation of crucial performance values, including torque, flux linkage and induced voltage. The comparisons with FEA results validate the model's effectiveness and applicability. (iv) Utility of multidomain network: The multidomain approach of the proposed model predicts flux density components independently, whilst maintaining physical relationships. This approach enhances the versatility and robustness of the model while improving the training efficiency compared to the separated network.

The proposed model has good potential for industrial deployment, particularly in applications that require repeated and rapid performance evaluations. By providing accurate electromagnetic field predictions and derived performance quantities within milliseconds, the proposed method can significantly accelerate the design workflow.

Despite its effectiveness, the proposed method has several limitations. The current framework is based on two-dimensional electromagnetic modelling and does not explicitly capture three-dimensional effects. The prediction accuracy also depends on the representativeness of the training dataset, and additional training or fine-tuning may be required when applying the model to new motor topologies, pole-slot configurations or material properties. Addressing these limitations will be the focus of future work.

Author Contributions

Mengyu Cheng: conceptualisation, data curation, formal analysis, investigation, methodology, resources, software, validation, visualisation, writing – original draft. **Xing Zhao:** conceptualisation, formal analysis, funding acquisition, investigation, project administration, supervision, validation, writing – review and editing. **Guangjin Li:** formal analysis, investigation, validation, writing – review and editing.

Funding

The work is funded by York Open Access Fund.

Conflicts of Interest

The authors declare no conflicts of interest.

Data Availability Statement

The data that support the findings of this study are available from the corresponding author upon reasonable request.

References

1. C. A. Stockton, R. F. McElveen, and E. Chastain, "The Integral Role of Electric Motors in Achieving Sustainability," *IEEE Transactions on Industry Applications* 60, no. 5 (September/October 2024): 7949–7957, https://doi.org/10.1109/TIA.2024.3408721.

2. W. Qiu, X. Zhao, A. Tyrrell, S. Perinpanayagam, S. Niu, and G. Wen, "Application of Artificial Intelligence-Based Technique in Electric Motors: A Review," *IEEE Transactions on Power Electronics* 39, no. 10 (October 2024): 13543–13568, https://doi.org/10.1109/TPEL.2024.3410958.

3. X. D. Sun, B. K. Wan, G. Lei, X. Tian, Y. G. Guo, and J. G. Zhu, "Multiobjective and Multiphysics Design Optimization of a Switched Reluctance Motor for Electric Vehicle Applications," (in English), *IEEE Transactions on Energy Conversion* 36, no. 4 (December 2021): 3294–3304, https://doi.org/10.1109/tec.2021.3078547.

4. J.-M. Jin, *The Finite Element Method in Electromagnetics* (John Wiley & Sons, 2015).

5. M. Cheng, X. Zhao, M. Dhimish, W. Qiu, and S. Niu, "A Review of Data-Driven Surrogate Models for Design Optimization of Electric Motors," *IEEE Transactions on Transportation Electrification* 10, no. 4 (December 2024): 8413–8431, https://doi.org/10.1109/TTE.2024.3366417.

6. Y. LeCun, Y. Bengio, and G. Hinton, "Deep Learning," *Nature* 521, no. 7553 (May 2015): 436–444, https://doi.org/10.1038/nature14539.

7. S. Doi, H. Sasaki, and H. Igarashi, "Multi-Objective Topology Optimization of Rotating Machines Using Deep Learning," (in English), *IEEE Transactions on Magnetics* 55, no. 6 (June 2019): 1–5, https://doi.org/10.1109/tmag.2019.2899934.

8. H. Sasaki and H. Igarashi, "Topology Optimization of IPM Motor With Aid of Deep Learning," (in English), *International Journal of Applied Electromagnetics and Mechanics* 59, no. 1 (2019): 87–96, https://doi.org/10.3233/jae-171164.

9. H. Sasaki and H. Igarashi, "Topology Optimization Accelerated by Deep Learning," (in English), *IEEE Transactions on Magnetics* 55, no. 6 (June 2019): 1–5, https://doi.org/10.1109/tmag.2019.2901906.

10. T. Aoyagi, Y. Otomo, H. Igarashi, H. Sasaki, Y. Hidaka, and H. Arita, "Prediction of Current-Dependent Motor Torque Characteristics Using Deep Learning for Topology Optimization," (in English), *IEEE Transactions on Magnetics* 58, no. 9 (September 2022): 1–4, https://doi.org/10.1109/tmag.2022.3167254.

11. H. Sasaki, Y. Hidaka, and H. Igarashi, "Prediction of IPM Machine Torque Characteristics Using Deep Learning Based on Magnetic Field Distribution," (in English), *IEEE Access* 10 (2022): 60814–60822, https://doi.org/10.1109/access.2022.3179835.

12. I. Goodfellow, J. Pouget-Abadie, M. Mirza, et al., "Generative Adversarial Networks," (in English), *Communications of the ACM* 63, no. 11 (November 2020): 139–144, https://doi.org/10.1145/3422622.

13. H. Wu, S. Niu, Y. Zhang, X. Zhao, and W. Fu, "Fast Magnetic Field Approximation Method for Simulation of Coaxial Magnetic Gears Using AI," *IEEE Journal of Emerging and Selected Topics in Industrial Electronics* 4, no. 1 (2023): 400–408, https://doi.org/10.1109/jestie.2022.3185558.

14. H. Wu, S. Niu, Y. Zhang, and W. Fu, "Physics-Informed Generative Adversarial Network-Based Modeling and Simulation of Linear Electric Machines," *Applied Sciences* 12, no. 20 (2022): 10426, https://doi.org/10.3390/app122010426.

15. Y. Pang, J. Lin, T. Qin, and Z. Chen, "Image-to-Image Translation: Methods and Applications," *IEEE Transactions on Multimedia* 24 (2021): 3859–3881, https://doi.org/10.1109/tmm.2021.3109419.

16. R. Zhong, Y. Xu, Y. Cao, et al., "Accurate Model of Switched Reluctance Motor Based on Indirect Measurement Method and Least Square Support Vector Machine," (in English), *IET Electric Power Applications* 10, no. 9 (November 2016): 916–922, https://doi.org/10.1049/iet-epa.2016.0112.

17. M. Khodapanah, A. F. Zobaa, and M. Abbod, "Estimating Power Factor of Induction Motors at Any Loading Conditions Using Support Vector Regression (SVR)," (in English), *Electrical Engineering* 100, no. 4 (December 2018): 2579–2588, https://doi.org/10.1007/s00202-018-0723-7.

18. Y. Shimizu, S. Morimoto, M. Sanada, and Y. Inoue, "Using Machine Learning to Reduce Design Time for Permanent Magnet Volume Minimization in IPMSMs for Automotive Applications," (in English), *IEEJ Journal of Industry Applications* 10, no. 5 (2021): 554–563, https://doi.org/10.1541/ieejjia.21004461.

19. Z. Pan, S. Fang, H. Wang, and Y. Zhong, "Accurate and Efficient Surrogate Model-Assisted Optimal Design of Flux Reversal Permanent Magnet Arc Motor," *IEEE Transactions on Industrial Electronics* 70, no. 9 (September 2023): 9312–9325. https://doi.org/10.1109/TIE.2022.3215444.

20. R. Savant, A. A. Kumar, and A. Ghatak, "Prediction and Analysis of Permanent Magnet Synchronous Motor Parameters Using Machine Learning Algorithms," in *2020 Third International Conference on Advances in Electronics, Computers and Communications (ICAECC)* (IEEE, 2020), 1–5.

21. A.-C. Pop, Z. Cai, and J. J. C. Gyselinck, "Machine-Learning Aided Multi-Objective Optimization of Electric Machines–Geometric-Feasibility and Enhanced Regression Models," *IEEE Journal of Emerging and Selected Topics in Industrial Electronics* 4, no. 3 (2023): 844–854, https://doi.org/10.1109/JESTIE.2023.3252404.

22. Y. M. You, "Multi-Objective Optimal Design of Permanent Magnet Synchronous Motor for Electric Vehicle Based on Deep Learning," (in English), *Applied Sciences-Basel* 10, no. 2 (January 2020): 482, https://doi.org/10.3390/app10020482.

23. S. Niu, T. Sheng, X. Zhao, and X. Zhang, "Operation Principle and Torque Component Quantification of Short-Pitched Flux-Bidirectional-Modulation Machine," *IEEE Access* 7 (2019): 136676–136685, https://doi.org/10.1109/access.2019.2942482.

24. H. Wu, Y. Zhang, W. Fu, C. Zhang, and S. Niu, "A Novel Pre-Processing Method for Neural Network-Based Magnetic Field Approximation," *IEEE Transactions on Magnetics* 57, no. 10 (2021): 1–9, https://doi.org/10.1109/tmag.2021.3095590.

25. S. Son, H. Lee, D. Jeong, K.-Y. Oh, and K. H. Sun, "A Novel Physics-Informed Neural Network for Modeling Electromagnetism of a Permanent Magnet Synchronous Motor," *Advanced Engineering Informatics* 57 (2023): 102035, https://doi.org/10.1016/j.aei.2023.102035.

26. C. Lee and W. Ha, "Optimal Design of IPM Rotor Shape Using Generative Adversarial Networks," in *2021 24th International Conference on Electrical Machines and Systems (ICEMS)* (IEEE, 2021), 2440–2444.

27. Y. Shimizu, S. Morimoto, M. Sanada, and Y. Inoue, "Automatic Design System With Generative Adversarial Network and Convolutional Neural Network for Optimization Design of Interior Permanent Magnet Synchronous Motor," *IEEE Trans Energy Convers* 38, no. 3 (2023): 724–734, https://doi.org/10.1109/TEC.2022.3208129.

28. F. I. Diakogiannis, F. Waldner, P. Caccetta, and C. Wu, "ResUNet-a: A Deep Learning Framework for Semantic Segmentation of Remotely Sensed Data," *ISPRS Journal of Photogrammetry and Remote Sensing* 162 (2020): 94–114, https://doi.org/10.1016/j.isprsjprs.2020.01.013.

29. T.-C. Wang, M.-Y. Liu, J.-Y. Zhu, A. Tao, J. Kautz, and B. Catanzaro, "High-Resolution Image Synthesis and Semantic Manipulation With Conditional Gans," in *Proceedings of the IEEE Conference on Computer Vision and Pattern Recognition* (2018), 8798–8807.